


Generation of rf radiation by low-intensity laser pulse trains in airGavin Blair  and Phillip Sprangle*Department of Physics, University of Maryland, College Park, Maryland 20742, USA;**Department of Electrical and Computer Engineering, University of Maryland, College Park, Maryland 20742, USA;
and Institute for Research in Electronics and Applied Physics, University of Maryland, College Park, Maryland 20740, USA*

(Received 15 February 2023; revised 13 April 2023; accepted 9 June 2023; published 14 July 2023)

In this paper, we analyze and numerically simulate mechanisms for generating directed rf radiation by a low-intensity laser pulse train (LPT) propagating in air. The LPT ionizes the air, forming a plasma filament. The ionization process relies on the background level of radioactivity which plays an important role in initiating a collisional ionization process. In our model a low-intensity LPT photoionizes background negative ions (produced by ambient ionizing radiation) and provides the seed electrons necessary to initiate collisional ionization. The intensity of the LPT is far below tunneling ionization levels. The ponderomotive forces associated with the LPT and self-fields drive plasma oscillations predominately in the radial direction. The driven radial electron currents in turn generate directed rf radiation. As the plasma density builds up on axis, the later portion of the LPT can defocus and limit the interaction length. The spectrum of the rf radiation consists of the fundamental frequency associated with the pulse separation time as well as harmonics. The rf generation mechanism is analyzed using fluid equations which incorporate, among other things, the effects of background radioactivity, photoionization, collisional ionization, ponderomotive and space-charge effects, and electron attachment–recombination processes. As an example, for a specific set of parameters, the rf spectrum and intensity are compared to experimental data.

DOI: [10.1103/PhysRevE.108.015203](https://doi.org/10.1103/PhysRevE.108.015203)**I. INTRODUCTION**

There has been a great deal of work done in recent decades on the generation of plasma filaments in air by high-intensity, ultrashort laser pulses [1–11]. In these studies, the laser pulse duration was typically in the multifemtosecond to picosecond regime and the intensities were high enough to induce tunneling ionization ($10^{18} - 10^{19}$ W/m²) in air. Recent work has shown that multiple laser pulses can be generated and used to generate extended plasma filaments [12,13]. For example, 30 laser pulses of duration ~ 30 fs, separated by ~ 0.5 ns and having a total energy of ~ 600 mJ, were used to generate plasma filaments in air [14].

Laser-plasma filament interactions have been used to generate terahertz (THz) radiation. For example, THz radiation has been produced by two-color laser pulses interacting in ionized air [15,16].

The generation of radiation by the interaction of laser pulses with plasma filaments is also of interest because of its potential applications in remote sensing, communications, and electronic countermeasures [15–20].

The present work focuses on the generation of radiofrequency (rf) radiation in air by low-intensity laser pulse trains (LPT). The O_2^- ions, which are generated by ambient levels of ionizing radiation, play a major role in the initiation of the plasma filaments. The negative ions are readily photoionized by the low-intensity LPT. For example, O_2^- ions have a low ionization potential, i.e., 0.46 eV [21], and are ionized by the low-intensity LPT. The photoionization of the negative ions provides seed electrons for collisional (avalanche) ionization to take place at relatively low laser intensities [19,20].

In this paper we analyze and numerically simulate a LPT propagating and ionizing air by a combination of photo- and collisional ionization processes. The ionized electrons are acted on by ponderomotive and space-charge forces and undergo oscillations predominately in the radial direction. The radial oscillating currents generate rf radiation. As micropulses propagate through the plasma filament, ponderomotive forces drive the electrons radially outward and space-charge forces tend to drive the electrons radially inward. The radial oscillating current density generates rf radiation in the forward and backward directions. The rf frequency spectrum is determined by the LPT repetition rate and micropulse duration. The fractional linewidth scales as the inverse of the number of micropulses in the LPT. For example, for a micropulse separation time of 650 ps, the fundamental rf frequency is 1.6 GHz. By varying the LPT repetition rate and micropulse duration, the rf frequency spectrum can be varied over a wide range.

We want to emphasize that this paper contains a number of inter-related mechanisms to generate tunable directed rf radiation using low-intensity laser pulse trains. Our proposed method has the potential to generate directed and tunable rf in the atmosphere at extended ranges. Preliminary experimental studies support our proposed rf generation mechanism. Since the rf wavelength can cover the entire global positioning system (GPS) spectrum, this approach has potential applications in electronic communications and countermeasures.

II. MODEL AND ANALYSIS

In our model the low-intensity LPT propagates in air and initiates photoionization of the ambient negative molecular

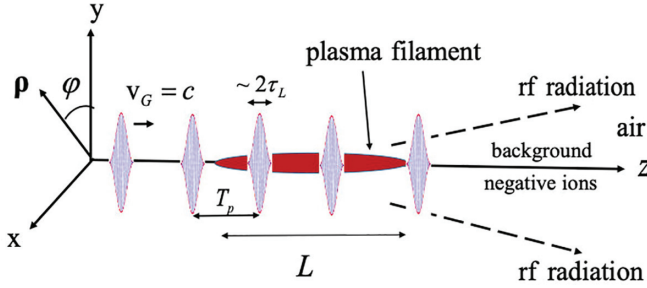


FIG. 1. Schematic overview of LPT generating a plasma filament in air by a combination of photoionization of background negative ions and collisional ionization processes. Radial plasma currents induced by ponderomotive LPT fields generate rf radiation in forward and backward directions.

ions, e.g., O_2^- ions. The photoionized electrons become the seed electrons for collisional ionization, which becomes the dominant ionization process after a few pulses of the LPT. The effective ponderomotive field associated with the LPT accelerates electrons radially outward, creating a radial space-charge field and radial current density. The space-charge field is created by the radial flow of electrons and the stationary positive ions. The space-charge field together with the ponderomotive field drive radial electron oscillations having a frequency related to the laser pulse separation time. The electron current is primarily in the radial direction and the rf radiation is directed primarily in the forward (backward) directions with a fundamental frequency given by $1/T_p$, where T_p is the micropulse separation time, as well as harmonics. The LPT undergoes defocusing as the plasma filament develops. This defocusing limits further ionization and limits the LPT-plasma interaction length. Figure 1 shows a schematic overview of the process of generating a plasma filament in the air through a combination of photoionization and collisional ionization from the LPT. The LPT and plasma fields induce currents that generate directed rf radiation.

A. Laser pulse train

The LPT interacts with the ionized plasma electrons in the region from $z = 0$ to $z = L$, where L is the length of the plasma filament. The LPT intensity consists of multiple, equally spaced micropulses. The micropulse intensity, in cylindrical geometry, is

$$I_{\text{pulse}}(\rho, \tau) = I_{\text{peak}} \exp(-2\rho^2/\rho_0^2) \exp(-2\tau^2/\tau_L^2), \quad (1)$$

where I_{peak} is the peak micropulse intensity, ρ_0 is the spot size, $\tau = t - z/c$, and τ_L is the micropulse duration. The energy in a single laser micropulse is given by $W_{\text{pulse}} = (\pi/2)^{3/2} \rho_0^2 \tau_L I_{\text{peak}}$.

The LPT consists of $N_p \gg 1$ micropulses separated in time by $T_p > \tau_L$. The Fourier series representation of the injected probe pulse train is

$$I_{\text{LPT}}(\rho, z, \tau) = I_0 \exp(-2\rho^2/\rho_0^2) \times \left[1 + \sum_{n=1}^{\infty} g_n \cos(\omega_n(\tau - \tau_L/2)) \right] T(\tau), \quad (2)$$

LPT Intensity (W/m^2) vs Time and Radius

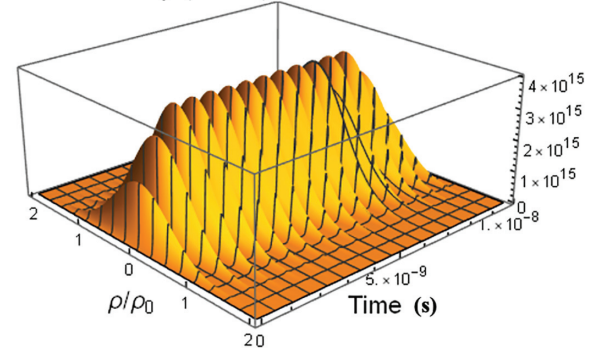


FIG. 2. LPT intensity I_{LPT} vs ρ/ρ_0 and $\tau = t - z/v_G$. Parameters for this plot are $I_{\text{peak}} = 4 \times 10^{15} \text{ W/m}^2$, $\tau_L = 100 \text{ ps}$, $T_p = 0.65 \text{ ns}$, $\rho_0 = 100 \mu\text{m}$, and $N_p = 15$.

where $I_0 = \sqrt{\pi/2}(\tau_L/T_p)I_{\text{peak}}$, the Fourier intensity coefficients are $g_n = 2 \exp[-(\omega_n \tau_L/2)^2/2]$, $\omega_n = 2\pi n/T_p$, $n = 0, 1, 2, \dots$, $T(\tau) = \Theta(\tau) - \Theta(\tau - T)$, and $\Theta(\tau)$ is a Heaviside step function. The LPT has an axial electric field which is neglected since its amplitude is down by the factor $\lambda_0/(2\pi\rho_0) \ll 1$. A typical plot of the LPT used in our simulations is shown in Fig. 2, where the laser parameters are taken from Table I.

B. Ponderomotive forces

The plasma currents that drive the rf radiation are induced by the ponderomotive forces associated with the LPT. The electromagnetic ponderomotive effective electric field (non-relativistic limit) is given by [22,23]

$$\mathbf{E}_{\text{pond}}(\mathbf{r}, t) = -\frac{q}{m\omega_0^2} \left(\frac{1}{2} \nabla(\mathbf{E} \cdot \mathbf{E}) \right), \quad (3)$$

where the terms on the right-hand side of Eq. (3) are averaged over an optical period, $I(\mathbf{r}, t) = n_0 |E(\mathbf{r}, t)|^2 / 2Z_0$ is the laser intensity, $Z_0 = \sqrt{\mu_0/\epsilon_0}$ is the vacuum impedance, $n_0 = ck_0/\omega_0$ is the index of refraction, ω_0 is the laser frequency, k_0 is the wave number, m is the electron mass, and q is the electron charge. The effective field in Eq. (3), in terms of the

TABLE I. Parameters used in simulations.

Parameter	
Peak laser intensity, I_{peak}	$4 \times 10^{15} \text{ W/m}^2$
LPT energy	150 mJ
Average LPT power	7.4 MW
Pulse length, τ_L	100 ps
Pulse separation time, T_p	650 ps
Number of pulses, N_p	25
LPT duration, T_{LPT}	16 ns
Spot size, ρ_0	100 μm
Peak pulse power, P_0	60 MW
Initial electron density, N_0	10^3 m^{-3}

laser intensity, is

$$\mathbf{E}_{\text{pond}}(\mathbf{r}, t) = -\frac{qZ_0}{2mn_0\omega_0^2} \nabla I(\mathbf{r}, t). \quad (4)$$

For the micropulse, with an intensity given by Eq. (1), the transverse and longitudinal components of the effective ponderomotive electric fields are, respectively,

$$E_{\text{pond},\rho} = E_P(\rho/\rho_0) \exp(-2\rho^2/\rho_0^2) \exp(-2\tau^2/\tau_L^2), \quad (5a)$$

$$E_{\text{pond},z} = E_P(\rho_0/v_G\tau_L)(\tau/\tau_L) \exp(-2\rho^2/\rho_0^2) \times \exp(-2\tau^2/\tau_L^2), \quad (5b)$$

where $E_P = 2qZ_0I_{\text{peak}}/(mn_0\omega_0^2\rho_0)$ and $v_G = c/n_0$ is the micropulse group velocity. For the parameters used in our simulations, the radial ponderomotive field dominates the longitudinal field. The ratio between the two is $E_{\text{pond},\rho}/E_{\text{pond},z} = (v_G\tau_L/\rho_0)^2(\rho/v_G\tau)$. In the parameter regime considered in this paper, $v_G\tau_L \gg \rho_0$, so that the radial ponderomotive force dominates by a few orders of magnitude.

In the case of the LPT, with an intensity given in Eq. (2), the transverse and longitudinal components of the effective ponderomotive electric field are, respectively,

$$E_{\text{LPT},\rho} = E_P \frac{I_0}{I_{\text{peak}}} \frac{\rho}{\rho_0} \exp(-2\rho^2/\rho_0^2) \times \left[1 + \sum_{n=1}^{\infty} g_n \cos(\omega_n(\tau - \tau_L/2)) \right] \Gamma(\tau), \quad (6a)$$

$$E_{\text{LPT},z} = \frac{E_P}{4} \frac{I_0}{I_{\text{peak}}} \frac{\rho_0}{v_G\tau_L} \exp(-2\rho^2/\rho_0^2) \times \sum_{n=1}^{\infty} g_n \omega_n \tau_L \sin(\omega_n(\tau - \tau_L/2)) \Gamma(\tau). \quad (6b)$$

C. Fluid model, driving current

The electron density, fluid velocity, and temperature equations are given by [17]

$$\frac{\partial N_e}{\partial \tau} + \frac{1}{\rho} \frac{\partial(\rho N_e V_\rho)}{\partial \rho} = Q_{\text{rad}} + \nu_{O_2^-} N_{O_2^-} + (\nu_{\text{col}} - \eta_A - \beta_e N_{\text{ion}}) N_e, \quad (7a)$$

$$\frac{\partial V_\rho}{\partial \tau} + V_\rho \frac{\partial V_\rho}{\partial \rho} = \frac{q}{m} [E_{\text{sc},\rho}(\rho, \tau) + E_{\text{pond},\rho}(\rho, \tau)] - \frac{V_\rho}{N_e} (Q_{\text{rad}} - \nu_{O_2^-} N_{O_2^-}), \quad (7b)$$

$$\frac{3}{2} \frac{\partial(N_e T_e)}{\partial \tau} = \langle \mathbf{J} \cdot \mathbf{E} \rangle - U_{\text{ion}} \frac{\partial N_e}{\partial \tau}, \quad (7c)$$

where N_e is the electron density, V_ρ is the radial electron fluid velocity, Q_{rad} is the background radioactivity ionization rate, $\nu_{O_2^-}$ is the photoionization rate of O_2^- ions, $N_{O_2^-}$ is the density of O_2^- ions, ν_{col} is the collisional ionization rate of neutral molecules, $\eta_A \approx 10^8[\text{s}^{-1}]$ is the electron reattachment rate, $\beta_e \approx 2 \times 10^{-14}[\text{m}^3/\text{s}]$ is the electron-ion recombination rate [24,25], N_{ion} is the positive ion density, $E_{\text{sc},\rho}$ is the radial space-charge field, $E_{\text{pond},\rho}$ is the effective radial ponderomotive field, i.e., Eq. (6a). In Eq. (7c), T_e is the electron

temperature in units of eV, $\langle \mathbf{J} \cdot \mathbf{E} \rangle$ is the ohmic heating due to the LPT, and U_{ion} is the average ionization potential for air, taken to be 14 eV. The ohmic heating term is given by $\langle \mathbf{J} \cdot \mathbf{E} \rangle = \omega_{pe}^2 \epsilon_0 E_{\text{eff}}^2 / 2\nu_e$ where $\omega_{pe} = (q^2 N_e / m \epsilon_0)^{1/2}$ is the plasma frequency, $E_{\text{eff}} = (\nu_e / \omega_0) E_0 / [1 + (\nu_e / \omega_0)^2]^{1/2}$ is the effective laser field, and $E_0 = (2Z_0 I_0 / n_0)^{1/2}$ is the peak laser field ($n_0 = 1$). In obtaining Eqs. (7a) and (7b), the thermal fluctuations in the fluid velocity are assumed to be small and are neglected. In addition, the magnitude of fluid velocity is $\ll c$, so that the pressure tensor and flux term in the time derivatives can be neglected. These approximations are checked and validated in our numerical simulations. For the range of parameters used in our simulations, the ambipolar diffusion coefficient is estimated to be $D_A \sim 10^{-3}[\text{m}^2/\text{s}]$ and the diffusion time $r_0^2/D_A \geq 1 \mu\text{s}$ [26]. The diffusion time is much longer than any time in the present process; therefore, diffusion effects are neglected.

The rate equations for the positive ion density, N_{ion} , and the negative ion density, $N_{O_2^-}$, are given by

$$\frac{\partial N_{\text{ion}}}{\partial \tau} = \nu_{\text{col}} N_e - (\eta_A + \beta_e N_e) N_{\text{ion}}, \quad (8a)$$

$$\frac{\partial N_{O_2^-}}{\partial \tau} = -\nu_{O_2^-} N_{O_2^-} + \eta_A N_e. \quad (8b)$$

The radial space-charge electric field is given by $(1/\rho)\partial(\rho E_{\text{sc},\rho})/\partial\rho = q(N_e - N_{\text{ion}})/\epsilon_0$. Using the continuity equation, $\partial(N_e - N_{\text{ion}})/\partial\tau = -(1/\rho)\partial(\rho N_e V_\rho)/\partial\rho$, the radial component of the space field is given by

$$\partial E_{\text{sc},\rho} / \partial \tau = -q N_e V_\rho / \epsilon_0. \quad (9)$$

In obtaining Eq. (9), the self-magnetic field has been neglected since the fluid velocities are $\ll c$.

In the absence of space charge and ionization, the maximum radial electron velocity from a micropulse due to the ponderomotive field in Eq. (6a) is $(V_{\rho,\text{pond}}/c)_{\text{max}} \approx I_0 \tau_L (r_e / \rho_0) \lambda_0^2 / (\pi m c^2)$, where $r_e = q^2 / (4\pi \epsilon_0 m c^2)$ is the classical electron radius. For example, if $I_0 = 10^{16} \text{W}/\text{m}^2$, $\rho_0 = 100 \mu\text{m}$, $\lambda_0 = 1 \mu\text{m}$, and $\tau_L = 100 \text{ps}$ the maximum radial electron velocity due to the ponderomotive force is $(V_{\rho,\text{pond}})_{\text{max}} \approx 10^{-4} c$. The velocity in the presence of space-charge fields is reduced.

Changes in air density due to thermal expansion are neglected in this model. The laser pulse train duration is $T \sim 10 \text{ns}$ and the spot size is $\rho_0 \sim 100 \mu\text{m}$. The air density depression due to the thermal blooming process occurs on a timescale of $\sim \rho_0 / v_s$, where $v_s \sim 300 \text{m}/\text{s}$ is the sound speed in air. The density depression time is $\rho_0 / v_s \sim 0.3 \mu\text{s}$, which is much longer than the laser pulse train duration.

As the electron plasma density increases, it can reach a level where the attractive radial space-charge force balances the repulsive radial ponderomotive force. When the increment in electron density caused by a single micropulse is large enough, the net radial force is substantially reduced. This balance occurs when the space-charge field is equal to the ponderomotive field.

D. Ionization and collision rates

Background ionizing radiation is the primary process through which negative ions are generated in air. Gamma rays, originating from cosmic and/or ground sources, can ionize air molecules. The ionized high-energy electrons cascade down to thermal energies and attach, for example, to oxygen molecules. A single MeV gamma ray can produce as many as $\sim 3 \times 10^4$ thermal electrons [7,27]. These electrons attach mainly to O_2 molecules to create O_2^- ions, which have a relatively long lifetime. The background radiation disintegration rate, at ground level, is $Q_{\text{rad}} \sim 10^7$ [pairs/(m³ - s)] which results in a negative ion density of $N_{O_2^-} \sim 3 \times 10^9 \text{m}^{-3}$ [7]. The background density of free electrons is, however, far less than the negative ion density. The ionization potential of O_2^- is 0.46 eV, while the photon energy for $\lambda_0 = 1 \mu\text{m}$ is 1.24 eV. Therefore, O_2^- ions can be ionized by single-photon ionization and thus, provide seed electrons for collisional ionization to further increase the electron density.

1. Photoionization

The photoionization rate for O_2^- is given by $\nu_{O_2^-} = \sigma_{\text{ion}} I / (\hbar \omega_0)$, where σ_{ion} is the ionization cross section, I is the intensity, and ω_0 is the frequency. The experimental value is $\sigma_{\text{ion}} \approx 5 \times 10^{-23} \text{m}^2$ for $\lambda_0 = 1 \mu\text{m}$ [21] and the single-photon ionization rate for O_2^- is $\nu_{O_2^-} [\text{s}^{-1}] = 2.5 \times 10^{-4} I(\rho, \tau) [\text{W}/\text{m}^2]$. This rate is sufficient to deplete the O_2^- ions in the optical volume for intensities in the range of $10^{15} - 10^{16} [\text{W}/\text{m}^2]$.

2. Collisional ionization

The collisional ionization rate in air can be written in the form [25,28] $\nu_{\text{col}} = \nu_{\text{col}}(N_2) + \nu_{\text{col}}(O_2)$, where the rates for N_2 and O_2 are $\nu_{\text{col}} = \nu_X (T_e/U_X)^{3/2} (U_X/T_e + 2) \exp(-U_X/T_e)$. ν_X is a characteristic frequency for species X , i.e., $\nu_{N_2} = 7.6 \times 10^{11} \text{s}^{-1}$, $\nu_{O_2} = 10^{11} \text{s}^{-1}$, T_e is the electron temperature in eV, and U_X is the molecular ionization potential for species X , i.e., $U_{N_2} \approx 15.6 \text{eV}$, $U_{O_2} \approx 12.1 \text{eV}$.

3. Collision frequency

The electron collision frequency is the sum of the electron-neutral and electron-ion collision frequencies, i.e., $\nu_e = \nu_{\text{en}} + \nu_{\text{ei}}$. The electron-neutral collision frequency [28] is given by $\nu_{\text{en}} [\text{s}^{-1}] = 2.8 \times 10^6 \sigma_n [\text{m}^2] N_n [\text{m}^{-3}] (T_e [\text{eV}])^{1/2}$, where $\sigma_n \approx 10^{-20} \text{m}^2$ is the molecular area. Setting the neutral molecular density equal to $N_n = N_{\text{air}} - N_e$, the electron-neutral collision frequency $\nu_{\text{en}} [\text{s}^{-1}] = 2.8 \times 10^{-14} (N_{\text{air}} [\text{m}^{-3}] - N_e [\text{m}^{-3}]) (T_e [\text{eV}])^{1/2}$, where $N_{\text{air}} = 2.7 \times 10^{25} \text{m}^{-3}$ is the air density. The electron-ion collision frequency is [28], for singly ionized plasmas, i.e., $N_i = N_e$, given by $\nu_{\text{ei}} [\text{s}^{-1}] = 2.9 \times 10^{-11} N_e [\text{m}^{-3}] (T_e [\text{eV}])^{-3/2}$, where the Coulomb logarithm was set equal to 10 and N_i is the positive ion density.

E. Defocusing of the laser pulse train

The electron plasma density is peaked on axis and, therefore, the refractive index is minimum on axis. The plasma filament, as well as diffraction, tends to defocus the micropulses in the LPT. To estimate the degree of defocusing,

we assume that the radial variation of the electron density near the axis is given by $N_e(\rho) \approx N_{e0}(1 - \rho^2/\rho_f^2)$, where $\rho < \rho_f$ is the characteristic radial size of the plasma filament. The plasma frequency, $\omega_{pe}(\rho) = [q^2 N_e(\rho)/m\epsilon_0]^{1/2}$, is peaked on axis. The axial variation of the laser field amplitude spot size $R(z)$ is given by [1]

$$\frac{\partial^2 R}{\partial z^2} = \frac{4c^2}{\omega_0^2 R^3} \left(1 + \frac{\omega_{p0}^2}{4c^2 \rho_f^2} R^4 - \frac{P}{P_{\text{NL}}} \right), \quad (10)$$

where $\omega_{p0} = \omega_{pe}(\rho = 0)$ is the plasma frequency on axis, P is the pulse power, and $P_{\text{NL}} = \lambda_0^2 / (2\pi n_L n_2)$ is the nonlinear focusing power [1,29]. The peak power P_0 in the micropulses is far below the nonlinear focusing power in air, i.e., $P_{\text{NL}} = \lambda_0^2 / (2\pi n_2) \sim 4 \text{GW}$, where $n_2 \approx 3 \times 10^{-23} \text{m}^2/\text{W}$ is the Kerr refractive index for air at $\lambda_0 = 1 \mu\text{m}$. Nonlinear focusing, therefore, has a negligible effect for our parameters. In addition, not shown in Eq. (10) is the relativistic focusing power [1,29], i.e., $P_{\text{rel}} = 17.4(\omega_0/\omega_{p0})^2 [\text{GW}]$, which is also far greater than the micropulse power and therefore does not contribute to focusing of the pulses. Plasma defocusing dominates both diffractive defocusing and nonlinear focusing for the parameters considered. Under these conditions, Eq. (10) reduces to $\partial^2 R / \partial z^2 = R / L_{\text{DF}}^2$, and the spot size is $R(z) = R(0) \exp(z/L_{\text{DF}})$, where $L_{\text{DF}} = (\omega_0/\omega_{p0})\rho_f$, is the defocusing length.

The peak micropulse intensity I_0 is no longer constant in the LPT but varies as

$$I_0(z) = I_0(0) \exp(-2z/L_{\text{DF}}), \quad (11)$$

due to defocusing.

When the electron density in the filament approaches air density ($2.7 \times 10^{25} \text{m}^{-3}$), the effect of plasma defocusing becomes significant. For example, when the plasma electron density approaches air density, the defocusing length $L_{\text{DF}} \sim 10^{-5} \text{m}$. Incoming micropulses will be able to maintain the high electron plasma density through ionization at the front of the filament, and the filament will continue to generate rf radiation at this elevated electron density.

F. rf radiation generation

The rf intensity and power generated by the plasma electrons interacting with the ponderomotive and self-fields associated with the LPT and plasma filament are obtained in this section. The radial ponderomotive and radial self-electric field are the dominant forces acting on the plasma electrons so that the driving current density is in the radial direction and the Poynting flux is primarily in the forward and backward axial directions. Although the electrons are essentially stationary axially, the ionizing process propagates in the forward direction. The rf frequency spectrum can be controlled by varying the repetition rate and micropulse duration of the LPT. The configuration used in obtaining the rf Poynting flux is shown in Fig. 3.

The vector potential associated with the rf in the radiation zone is reduced to

$$\mathbf{A}(\mathbf{r}, t) = \frac{\mu_0}{4\pi r} \int_V \mathbf{J}(\mathbf{r}', t - r/c + \mathbf{r}' \cdot \hat{\mathbf{r}}/c) d^3 \mathbf{r}', \quad (12)$$

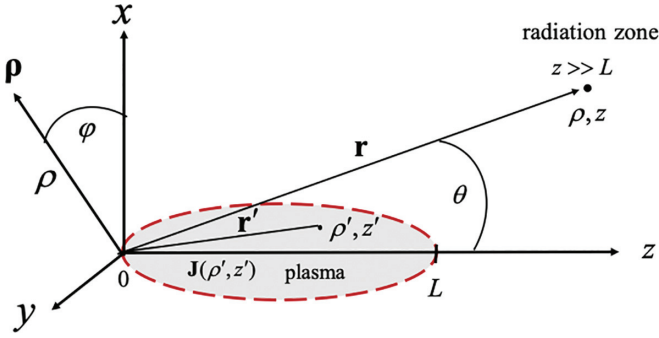


FIG. 3. Configuration used in evaluation of rf intensity. Localized current and charge density are confined to region with dotted red curve.

where \mathbf{J} is the radial current density and the integration is over the current density source, $d^3\mathbf{r}' = \rho' d\rho' d\varphi' dz'$. In the radiation zone the fields are $\mathbf{E}(\mathbf{r}, t) = \hat{\mathbf{r}} \times (\hat{\mathbf{r}} \times \partial\mathbf{A}/\partial t)$ and $\mathbf{B}(\mathbf{r}, t) = -c^{-1}\hat{\mathbf{r}} \times \partial\mathbf{A}/\partial t$, where $\hat{\mathbf{r}}$ is the radial unit vector from the origin. The Poynting flux associated with the rf radiation is given by

$$\mathbf{S}(\mathbf{r}, t) = (1/Z_0)|\hat{\mathbf{r}} \times \partial\mathbf{A}(\mathbf{r}, t)/\partial t|^2\hat{\mathbf{r}}, \quad (13)$$

where $Z_0 = \sqrt{\mu_0/\epsilon_0}$. The angular distribution of the rf power is given by $dP(\mathbf{r}, t)/d\Omega = r^2\mathbf{S}(\mathbf{r}, t) \cdot \hat{\mathbf{r}}$, where $d\Omega = \sin\theta d\theta d\varphi$, and the total power radiated is $P = r^2 \int \mathbf{S}(\mathbf{r}, t) \cdot \hat{\mathbf{r}} d\Omega$. The radial component of the vector potential in the radiation zone is

$$\mathbf{A}(\rho, z, t) = \frac{\mu_0}{2r} \int_0^L \int_0^\infty \mathbf{J}(\rho', z', t_R) \rho' d\rho' dz', \quad (14)$$

where the radial current density is $\mathbf{J} = qN_e V_\rho \hat{\rho}$, $t_R = t - r/c + (\rho' \sin\theta + z' \cos\theta)/c$ is the retarded time, $\rho = r \sin\theta$ and $z = r \cos\theta$. The current density $J = qN_e V_\rho$ is obtained by numerically solving Eqs. (7a)–(7c), (8a), (8b), and (9).

The angular power distribution is given by

$$dP(\mathbf{r}, t)/d\Omega = r^2 Z_0^{-1} |\hat{\mathbf{r}} \times \partial\mathbf{A}(\mathbf{r}, t)/\partial t|^2 = r^2 Z_0^{-1} |\mathbf{E}(\mathbf{r}, t)|^2, \quad (15)$$

and is independent of r .

III. SIMULATION RESULTS

In this section, Eqs. (7a)–(7c) together with Eqs. (8a), (8b), and (9) are solved numerically for the electron density and the radial space-charge field. Equation (9) is used to evaluate the radial current density. At the end of the LPT, the radial space-charge field balances the radial ponderomotive field, i.e., $E_{sc,\rho} \approx -E_{pond,\rho}$. This approximation is used to simplify the simulations at the tail end of the LPT. The radial plasma current density is used in Eq. (14) to obtain the vector potential associated with the rf radiation in the radiation zone. The Poynting flux and angular distribution of the radiation are obtained using Eqs. (13) and (15), respectively. These equations were solved using the various programs in *Mathematica 12.0*. The parameters used in the simulations are given in Table I.

The energy depletion of the LPT can be neglected in the ionization process, since the energy needed to ionize the air is significantly less than the LPT energy.

A. Atmospheric LPT propagation

Here, the LPT propagates into air and photoionizes the ambient negative ions to initiate collisional ionization. Figure 4(a) shows the electron density, N_e , on axis as a function of time. Figure 4(b) shows the electron density as a function of time and radius. The maximum electron density reached by the plasma filament is $\sim 10^{25} \text{ m}^{-3}$. The electron density is localized on axis and increases toward the end of the LPT. The space-charge electric field is less than the ponderomotive field at the beginning of the LPT. Therefore, there is little restoring force on the electrons. Once the space-charge electric field becomes comparable to the ponderomotive field, the electron fluid velocity and the current density reach a maximum. Figure 5(a) shows the electron current density as a function

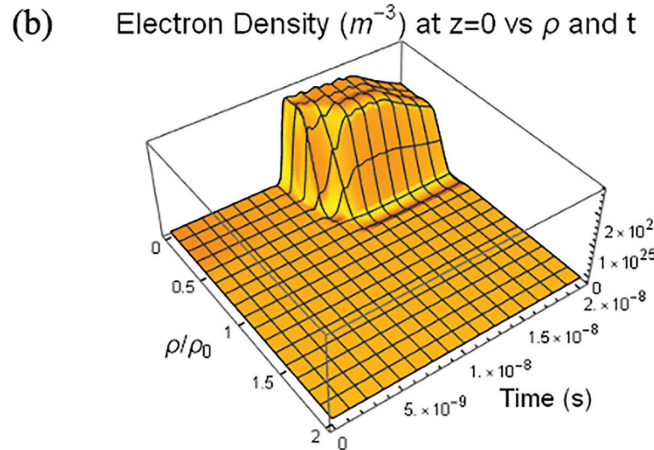
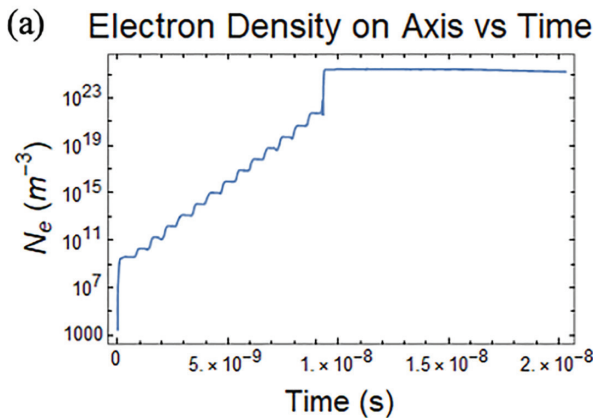


FIG. 4. Electron density as a function of time in laser pulse frame for a LPT with 25 micropulses. Peak laser intensity is $I_0 = 4 \times 10^{15} \text{ W/m}^2$. (a) Logarithmic plot of electron density along axis of propagation. (b) Electron density as a function of time and radius, normalized to spot size, from axis of propagation.

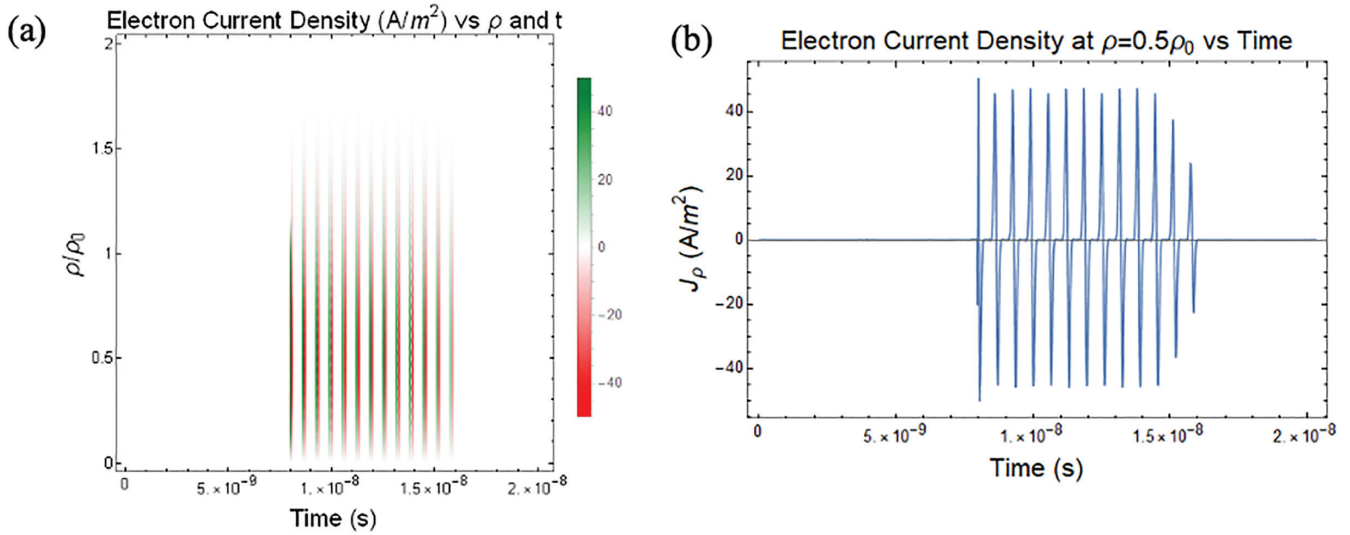


FIG. 5. Radial electron current density for a LPT of 25 micropulses having a peak intensity of $I_0 = 4 \times 10^{15}$ W/m². (a) Radial current density as a function of radius, normalized to spot size, and time in laser pulse frame. (b) Radial electron current density as a function of time in laser pulse frame at $\rho = 0.5\rho_0$.

of radius and time. The current density is highest near the end of the LPT, where the electron density is high and the space-charge field is comparable to the ponderomotive field. Figure 5(b) shows the electron current density at $\rho = 0.5\rho_0$ as a function of time.

B. rf radiation generation

Figure 6 shows a comparison of our simulated rf spectrum with an experimental spectrum [13,17] employing very similar LPT parameters. The experiment employed a LPT consisting of >30 micropulses with a micropulse separation of $T_p = 650$ ps. The focused LPT, having a total energy of $E_{LPT} = 510$ mJ, generated a plasma filament in air. The peak intensity of the micropulses is estimated to be $I_{peak} \approx 5 \times 10^{15}$ W/m². A loop antenna was used to detect the rf signal generated by the plasma filament [13,17]. Figure 6(a)

shows the spectrum by taking a Fourier transform of Eq. (13). The peak intensity of the total calculated rf signal, approximately half a meter from the filament, is $\sim 10^{-10}$ W/m² ($E_{rf} \sim 10^{-4}$ V/m). Preliminary experimental results, using a loop antenna, indicate that the peak rf electric field is $E_{rf} \sim 10^{-4}$ V/m. Figure 6(b) shows the experimental spectrum. The antenna in the experiment is tuned to receive a narrow range of frequencies. Therefore, harmonics that are present in the calculated spectrum are not shown in the experimental data.

The angular dependence of the radiation for plasma filaments of varying lengths is shown in Fig. 7. Figure 7 shows the peak rf intensities of the Poynting flux given by Eq. (13). For short filament lengths, i.e., $L < \lambda_{rf}$, where λ_{rf} is the wavelength of the rf, there is significant radiation directed in the backward direction, as well as the forward direction. In our parameter regime, the plasma defocusing of the LPT limits the length of the filament to be $< \lambda_{rf}$.

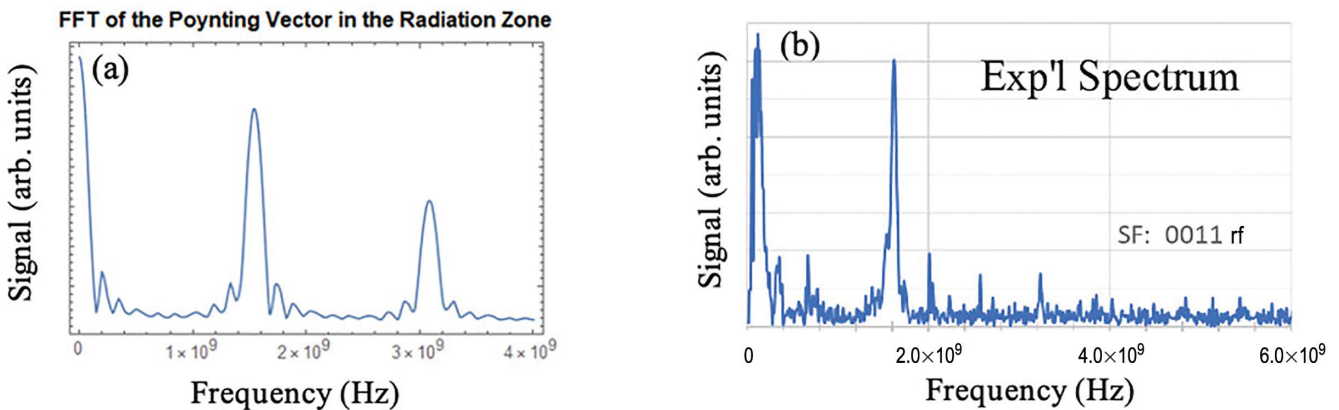


FIG. 6. Calculated and experimental spectra of the rf in arb. units. (a) Calculated spectrum from a LPT with 40 micropulses and (b) experimentally measured spectrum. Fundamental peak is at 1.6 GHz in both spectra. Note that harmonics are not shown in experimental spectrum since receiving antenna was tuned to only a narrow range of frequencies. Harmonics, however, have been measured experimentally (private communications with V. Markov at AS&T, Inc. [13]).

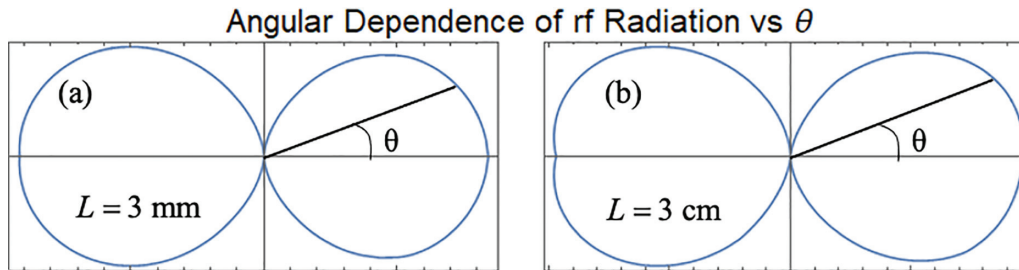


FIG. 7. Polar plots showing dependence of strength of rf signal on angle θ for various plasma filament lengths: (a) 3 mm and (b) 3 cm.

IV. SUMMARY AND DISCUSSION

In this paper, we proposed, analyzed, and numerically simulated a mechanism for generating rf radiation in air by using low-intensity laser pulse trains. In our model, the LPT propagates in air and photoionizes the ambient negative molecular ions, which are present due to background (ambient) radiation. The photoionized electrons provide the seed electrons for collisional ionization to take place and become the dominant ionization process. The buildup of electrons forms a plasma filament. The ionized plasma electrons are acted on by the ponderomotive forces (radial and axial) associated with the LPT. For the parameters considered, the radial electron oscillations driven by the LPT ponderomotive and self-fields dominate. The formation of the plasma filament tends to defocus the trailing pulses in the LPT, which can limit the length of the plasma filament. The radial plasma oscillations provide a driving current density which generates rf radiation primarily in the forward (backward) directions. The duration of the rf signal is determined by the duration of the LPT.

The peak intensity of the rf signal, approximately half a meter from the filament, is $\sim 10^{-10}$ W/m² ($E_{\text{rf}} \sim 10^{-4}$ V/m), which is in agreement with the experimentally measured rf field. The frequency spectrum of the rf radiation is determined by harmonics of the micropulse separation time and duration. The frequency spectrum can be controlled by varying the pulse repetition rate and duration of the micropulses. For a particular set of LPT parameters, our numerically simulated frequency spectrum is in general agreement with the experimental spectrum.

ACKNOWLEDGMENTS

The authors would like to thank Dr. Vladimir Markov for valuable discussions concerning the experimental spectrum obtained at AS&T Laboratories. In addition, we thank Q. Saulter of ONR for providing useful suggestions and funding of this work. We would also like to thank ARO for funding of this work.

-
- [1] P. Sprangle, J. R. Peñano, and B. Hafizi, *Phys. Rev. E* **66**, 046418 (2002).
 - [2] P. Sprangle, J. R. Peñano, B. Hafizi, and C. A. Kapetanakis, *Phys. Rev. E* **69**, 066415 (2004).
 - [3] X. Liu *et al.*, *Opt. Express* **20**, 5968 (2012).
 - [4] S. Eisenmann, J. Peñano, P. Sprangle, and A. Zigler, *Phys. Rev. Lett.* **100**, 155003 (2008).
 - [5] S. Varma, Y.-H. Chen, and H. M. Milchberg, *Phys. Rev. Lett.* **101**, 205001 (2008).
 - [6] A. Ting, I. Alexeev, D. Gordon, E. Briscoe, J. Peñano, R. Fischer, R. Hubbard, P. Sprangle, and G. Rubel, *Appl. Opt.* **44**, 5315 (2005).
 - [7] A. J. Peurrung, *Nucl. Instrum. Methods. Phys. Res. A* **481**, 731 (2002).
 - [8] Y. E. Geints and A. A. Zemlyanov, *J. Opt. Soc. Am. B* **31**, 788 (2014).
 - [9] Y. E. Geints and A. A. Zemlyanov, *Appl. Opt.* **56**, 1397 (2017).
 - [10] A. Houard, V. Jukna, G. Point, Y.-B. André, S. Klingebiel, M. Schultze, K. Michel, T. Metzger, and A. Mysyrowicz, *Opt. Express* **24**, 7437 (2016).
 - [11] A. Schmitt-Sody, H. Kurz, L. Bergé, S. Skupin, and P. Polynkin, *New J. Phys.* **18**, 093005 (2016).
 - [12] Y. E. Geints and A. A. Zemlyanov, *Atmos. Ocean Opt.* **31**, 112 (2018).
 - [13] V. Markov (private communications).
 - [14] D. Reyes, H. Kerrigan, J. Peña, N. Bodnar, R. Bernath, M. Richardson, and S. R. Fairchild, *J. Opt. Soc. Am. B* **36**, G52 (2019).
 - [15] D. J. Cook and R. M. Hochstrasser, *Opt. Lett.* **25**, 1210 (2000).
 - [16] K. Y. Kim, J. H. Glowina, A. J. Taylor, and G. Rodriguez, *Opt. Express* **15**, 4577 (2007).
 - [17] G. Blair, V. Markov, and P. Sprangle, Generation of RF radiation by laser pulse trains in air, *Proc. SPIE* **12237**, 1223706 (2022).
 - [18] S. A. Uryupin and A. A. Frolov, *J. Exp. Theor. Phys.* **114**, 878 (2012).
 - [19] M. N. Shneider and R. B. Miles, *Appl. Phys. Lett.* **101**, 264105 (2012).
 - [20] C. D'Amico, A. Houard, M. Franco, B. Prade, and A. Mysyrowicz, *Opt. Express* **15**, 15274 (2007).
 - [21] L. G. Christophorou, *Atomic and Molecular Radiation Physics* (Wiley-Interscience, London, New York, 1971), p. 530.
 - [22] J. Jackson, *Classical Electrodynamics* (Wiley, New York, 1998).

- [23] A. Zangwill, *Modern Electrodynamics* (Cambridge University Press, New York, 2012).
- [24] P. Sprangle, B. Hafizi, H. Milchberg, G. Nusinovich, and A. Zigler, *Phys. Plasmas* **21**, 013103 (2014).
- [25] J. Isaacs, C. Miao, and P. Sprangle, *Phys. Plasmas* **23**, 033507 (2016).
- [26] E. S. Tanenbaum, *Plasma Physics* (McGraw-Hill, Blacklick, OH, 1967).
- [27] Y. S. Dimant, G. S. Nusinovich, P. Sprangle, J. Penano, C. A. Romero-Talamas, and V. L. Granatstein, *J. Appl. Phys.* **112**, 083303 (2012).
- [28] Y. B. Zel'dovich and Y. P. Raizer, *Physics of Shock Waves and High Temperature Hydrodynamic Phenomena* (Dover, Mineola, NY, 2002), pp. 342, 388, 389.
- [29] R. Boyd, *Nonlinear Optics* (Academic Press, San Diego, 2008).